Axial load detection in compressed steel beams using FBG–DSM sensors

Marco Bonopera*[1,3a], Kuo-Chun Chang[2b], Chun-Chung Chen[1c], Zheng-Kuan Lee[1d] and Nerio Tullini[3e]

[1]*Bridge Engineering Division, National Center for Research on Earthquake Engineering, Taipei, Taiwan*
[2]*Department of Civil Engineering, National Taiwan University, Taipei, Taiwan*
[3]*Department of Engineering, University of Ferrara, Ferrara, Italy*

(Received , Revised , Accepted)

Abstract. Nondestructive testing methods are required to assess the condition of civil structures and formulate their maintenance programs. Axial force identification is required for several structural members of truss bridges, pipe racks, and space roof trusses. An accurate evaluation of *in situ* axial forces supports the safety assessment of the entire truss. A considerable redistribution of internal forces may indicate structural damage. In this paper, a novel compressive force identification method for prismatic members implemented using static deflections is applied to steel beams. The procedure uses the Euler–Bernoulli beam model and estimates the compressive load by using the measured displacement along the beam's length. Knowledge of flexural rigidity of the member under investigation is required. In this study, the deflected shape of a compressed steel beam is subjected to an additional vertical load that was short-term measured in several laboratory tests by using fiber Bragg grating–differential settlement measurement (FBG–DSM) sensors at specific cross sections along the beam's length. The accuracy of midspan deflections offered by the FBG–DSM sensors provided excellent force estimations. Compressive load detection accuracy can be improved if substantial second-order effects are induced in the tests. In conclusion, the proposed method can be successfully applied to steel beams with low slenderness under real conditions.

Keywords: deflected shape; FBG–DSM sensor; force identification; inverse problem; static test; steel beam

1. Introduction

Knowledge of the displacement field of a structure is crucial for assessing the structure's safety (Aldar 2013). Direct measurement techniques such as using linear variable differential transformers or dial indicators require fixed references below the measurement points, which are difficult to apply in practice. By contrast, the accuracy of the traditional geodetic technique is generally limited by measurement errors of few millimeters. The hydrostatic leveling system comprises communicating vessels filled with an appropriate liquid fixed to the structure at selected points. As a rule regarding fixed supports, one vessel of the circuit is designated as the datum reference. The constant absolute altitude of the liquid-free surface is ensured by the hydrostatic equilibrium of the communicating vessels. Consequently, vertical displacements can be obtained by measuring the liquid height variation in each vessel. Typically, a resolution of few tenths of a millimeter can be obtained. Sensors proposed for practical application differ in terms of how the liquid level is measured (Marecos 1978, Vurpillot *et al*. 1998, International Federation for Structural Concrete 2003, Rodrigues *et al.* 2010, Rodrigues *et al.* 2011 and the references cited therein). In particular, in Rodrigues *et al.* (2010, 2011), fiber Bragg grating (FBG)-based sensors connected to a float on the liquid have been used as transducer load cells to measure the apparent immersed weight of a suspended float, which is a linear function of the liquid level inside the sensor. The FBG–differential settlement measurement (DSM) (FBG–DSM) sensor used in this paper employs prestressed clamped FBG with a direct connection to the immersed float, as illustrated in patents (Lee 2014, 2015). Lai *et al.* (2016) used the same FBG mechanism for liquid-level sensors to conduct railway track differential settlement measurements. The mechanism of this FBG–DSM sensor can provide reliable measurement results of the deflected shapes of structures. One aim of the present study was to estimate the accuracy of this type of FBG–DSM sensor when applied to a compressed steel beam to simulate more rugged conditions than those of a calibration test. The main purpose of this study was to simulate the field procedure of a novel nondestructive testing (NDT) method for detecting the axial load in a compressed steel beam base d on the displacement measured along the beam's length.

In situ structural assessment of compressive forces is required in the top chords of truss bridges, pipe racks, and space roof trusses. These structures require operating state control to support safety assessments during their serviceability. A considerable redistribution of internal forces

*Corresponding author, Ph.D., E-mails: bonopera@ncree.narl.org.tw – marco.bonopera@unife.it
[b]Professor, E-mail: ciekuo@ntu.edu.tw
[c]Ph.D., E-mail: ccchen@ncree.narl.org.tw
[d]Ph.D., E-mail: zklee@ncree.narl.org.tw
[e]Professor, E-mail: nerio.tullini@unife.it

may indicate damage. Nondestructive static and dynamic methods have been studied for axial force identification in externally loaded beams (Tullini and Laudiero 2008, Bahra and Greening 2011, Tullini *et al.* 2012, Tullini 2013, Rebecchi *et al.* 2013, Maes *et al.* 2013, Bonopera *et al.* 2018 and the references cited therein). In particular, vibration-based estimations of axial loads require accurate selection of the flexural mode shape for use in the identification process (Bahra and Greening 2011, Maes *et al.* 2013). Such methods are particularly sensitive to experimental and model errors. Moreover, selecting *a priori* the optimal frequency for estimating the axial load is difficult, and different natural frequencies yield different degrees of accuracy in axial force estimations. Lim and Soh (2013) and Naseralavi *et al.* (2016) have studied dynamic methods for damage detection in axially loaded beams. In these methods, load predictions are mainly affected by numerical and experimental errors due to the level of noise.

In this study, a novel NDT method for compressive load detection in prismatic beams was applied to steel members. A posttensioned steel beam with a straight unbonded tendon was utilized as a prototype for experimental and numerical simulations. The reference model comprised a simply supported Euler–Bernoulli beam compressed by a straight unbonded tendon, where compressive force was modeled as an external axial load applied eccentrically to the beam ends. In this framework, the total vertical displacement from a three-point bending test is accurately approximated by multi -plying the first-order deflection by the magnification factor of the second-order effects (Timoshenko and Gere 1961, Bazant and Cedolin 1991), as predicted using the "compression-softening" theory in the static case. First, deflected shape measurements obtained from 33 three-point bending tests were used to assess the accuracy of the FBG–DSM sensors. Reliability was verified by comparing their measurements with recorded displacements by using dial indicators positioned at specific cross sections along the beam's length. Second, deflections obtained from 24 additional three-point bending tests were concurrently recorded using the same FBG–DSM sensors to verify the ac curacy of the beam mechanical model assumption. Minor displacements were imposed in the experiments to preserve the beam in the elastic range. Subsequently, the aforementio ned magnification factor approach based on the "compression-softening" theory was profitably employed to detect the compressive loads by using one measured deflection only. All compressive forces maintained their original lines of action and did not vary the eccentricity of the force with respect to the beam axis when the deflected shapes were imposed. The NDT method involves estimating the compressive load by measuring one displacement along the element's length after applying a vertical load. Furthermore, knowledge of the flexural rigidity of the steel beam under investigation is required. This technique uses static parameters only. Reliable compressive force detection based on the accurate midspan measurements obtained by the FBG–DSM sensors confirms the robustness of the method. This method can be applied to generic prismatic steel members if the stiffnesses of the boundary conditions are known.

2. FBG–DSM sensors

Optical fibers are a transmission medium of light energy or signals. These intrinsic fiber sensors are based on the optical properties of processed or unprocessed fibers such as Brillouin sensors, Raman sensors, and evanescent sensors. In this study, intrinsic optical fibers exposed to artificial ultraviolet irradiation were used to form FBGs by employing phase masks with the corresponding reflected central wavelength of the FBGs. Changes in stress (strain) and temperature engender changes in the central wavelength of FBGs, which can be analyzed using a signal-processing device to convert the reflected signals. Therefore, FBGs are sensing components and have sensing functionality. Through a mechanical procedure, FBGs can be used to designate sensing devices such as strain or displacement sensors for various purposes. For example, Kim *et al.* (2011) and Sung *et al.* (2017) have designed FBG sensors embedded in prestressing tendons to measure the applied tension force and load transfer along a tendon's length.

The key process method proposed by the National Center for Research on Earthquake Engineering is to clamp the optical fiber with heat shrinkable sleeves for a total length of 140 mm, expressed as S1 + FBG + S2 (Fig. 1), which are used as connectors between the bare fiber and additional element to introduce external forces into the FBG. This innovative design enhances the stability of the internal component of the FBG–DSM sensors. Using these connectors, instrument components can exert prestress, which serves as the sensing origin (Fig. 1). In particular, the FBG–DSM sensor comprises a suspended mass, FBGs, and two sleeves. One sleeve is directly connected to the suspended float mass and the other one is connected to the upper fixed end of the customized container (vessel), as shown in Fig. 2. The layout of the FBG–DSM sensor system is illustrated in Fig. 3; the communicating vessels contain a homogeneous fluid and the elastic range of FBGs is governed by floating mechanics and Hooke's law. According to the buoyancy principle, the magnitude of the buoyancy force is equal to the weight of an equal volume of fluid. Therefore, as the immersed volume of the suspended object increases, the force detected by FBG from pulling the suspended object changes. In particular, the maximum prestress force of the fiber is equal to the weight of the floating body (suspended mass) minus half of the volume of the floating body multiplied by the water density. Variations in water surface height do not affect the overcoming of the ultimate tensile strength of the optical fiber. The main properties of the fiber in the FBG–DSM sensors used in this study are listed in Table 1.

Several FBG–DSM sensors can be linked using a connecting pipe. When a FBG–DSM sensor displaces downwar d with the structure, the suspended cylindrical object within the sensor (with higher density than the liquid) also moves d ownward; however, its liquid surface moves relatively upwa rd inside the sensor until the same liquid surface has been ob tained within the connected FBG–DSM sensors. Therefore,

changes in the buoyancy of the floats alter the force exerted on the FBG, thereby changing the reflective light wave length. With respect to the linear behavior of the FBG material, the mathematical expression for the FBG–DSM sensor can be expressed as follows:

$$\begin{aligned}&\Delta(\textit{liquid surface height}) \propto \Delta(\textit{buoyancy}) \propto \\ &\propto \Delta(\textit{fiber stress}) \propto \Delta(\textit{fiber strain}) \propto \\ &\propto \Delta(\textit{the central wavelength of the reflective light}).\end{aligned} \tag{1}$$

The logger can be placed on the ground, whereas the optical wires run externally and internally through the FBG–DSM sensors. Once the data logger instrument has measure d the Δ (central wavelength of the reflective light), the Δ (liquid surface height) can be obtained (Eq. 1), thereby enabling the corresponding vertical displacement to be obtained.

The nominal stroke of the adopted FBG–DSM sensor was 40 mm. Therefore, the range of the displacement measurement was able to be calculated. A linear change in the wavelength was observed because of the internal dimensions of the suspended cylindrical object and customized volume of the packaging case of the FBG–DSM sensor. When the maximum stroke was 40 mm, the elongation of the used fiber was approximately 0.11 mm with a wavelength shift of 3.25 nm. The ultimate elongation of the fiber corresponding to its ultimate tensile strength was approximately 0.20 mm, corresponding to a wavelength shift of approximately 6 nm (value obtained from the uniaxial tensile test performed on the fiber).

In long-term monitoring, one FBG–DSM sensor should be used in the stress-free state to determine the influence of temperature and eliminate the temperature effects of the other connected FBG–DSM sensors. In short-term monitoring, the temperature effect can be rationally overlooked if the temperature's level of influence does not exceed the critical value of 10%. More details are provided in patents (Lee 2014, 2015) and preliminary field tests on bridges using the FBG–DSM sensors are described in Chang *et al.* (2012), Lee (2013) and Lee *et al.* (2014). Every conventional electronic sensor requires individual wires connected to the data acquisition instrument or remote transmission module. Therefore, complicated wire connections are usually required when numerous electronic sensors are applied. One of the main advantages of optical sensing technology is the plain connection of the sensors enabled by FBGs with different reflection wavelengths connected in series by using a single transmission optical fiber. Fig. 3 shows a series of FBG–DSM sensors; additional sensors can be connected in one channel depending on the wavelength band of the instrument's input light as well as splice fusion for the optical fiber. With careful splice fusion, generally, one fiber can contain approximately 20 FBG-based sensors. The FBG–DSM sensors can be appropriately deployed *in situ* in structures such as concrete bridge decks, truss bridges, pipe racks, pipelines, and viaducts. Short- or long-term monitoring systems with a series of FBG–DSM sensors can provide near-simultaneous elevation profiles or structures with vertical deflected shapes.

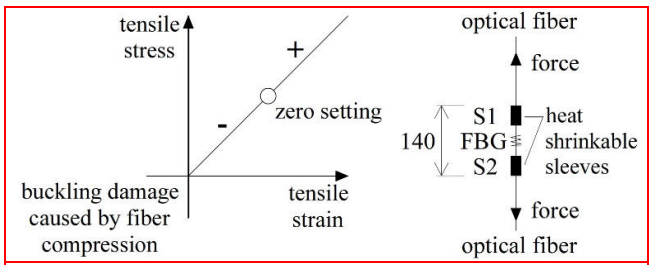

Fig. 1 Exerting prestress and setting sensing origin (left). Connector introducing external force into the FBG (Lee 2014, 2015). Units in mm (right)

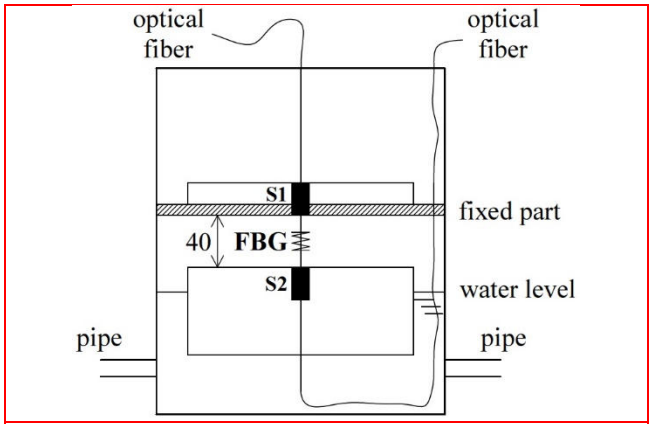

Fig. 2 Internal system of the employed FBG–DSM sensor (Lee 2014, 2015). Units in mm

Table 1 Main properties of the optical fiber installed inside the employed FBG–DSM sensor (Lee 2014, 2015)

Fiber type	single-mode optical fiber
Fiber coating	acrylate
Fiber grating length	15 mm
Fiber grating width spectral reflectivity	93.87%
Center wavelength	1526.963 nm
Strain optic coefficient	$0.78 \times 10^{-6}/\mu\varepsilon$
Ultimate tensile elongation	≈ 0.20 mm
Wavelength shift (corresponding to the ultimate tensile elongation)	≈ 6 nm

2.1. Numerical example of measured displacement using the FBG–DSM sensor

The FBG–DSM sensor used in this study can provide settlement measurements with a tolerance of 0.01 mm from the change in wavelength of the fiber within the vessel (Lee 2014, 2015). The liquid height variation of the water inside the tank produces a difference in the wavelength of the installed fiber. The analytical manipulations of a measurement example are illustrated in this section.

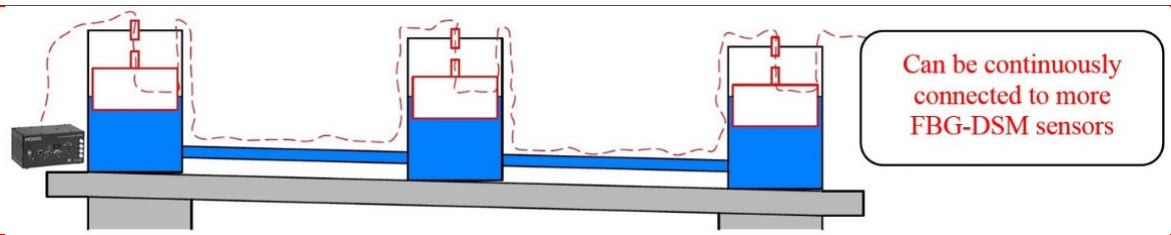

Fig. 3 Layout of the employed FBG–DSM sensor system

The diameter D of the cylindrical mass float inside the FBG–DSM sensor is equal to 48.0 mm, whereas the water height variation Δh is assumed to be 12.30 mm. The change in water volume ΔV surrounding the suspended float is obtained through Equation (2).

$$\Delta V = \frac{\pi^2 D^2}{4}\Delta h = \frac{\pi^2 48.0^2}{4} \times 12.30 = 7*10^4 \text{ mm}^3. \quad (2)$$

The tensile force Δf in the fiber, expressed in gram-force [gW], can be subsequently obtained using Equation (3), where D_w represents the water density.

$$\Delta f = \Delta V \; D_w = 7*10^4 \times 0.001 = 70 \text{ gW}. \quad (3)$$

The uniaxial tensile test conducted using a universal testing machine on the fiber installed inside the sensor reveals that $\Delta\lambda$ = 1 nm wavelength shift corresponds to an applied tensile force of 70 gW. Thus, if the assumed water height variation Δh is 12.30 mm, the corresponding wavelength $\Delta\lambda$ of the fiber is equal to 1 nm. Subsequently, from the center wavelength value, λ_B = 1527 nm, and strain optic coefficient of the fiber used, $C_{s\Delta\varepsilon} = 0.78 \times 10^{-6}$ / με, the strain $\Delta\varepsilon$ in the fiber can be obtained using Equation (4).

$$\Delta\varepsilon = \frac{\Delta\lambda}{\lambda_B}\frac{1}{C_{s\Delta\varepsilon}} = \frac{1}{1527} \times \frac{1}{0.78 \times 10^{-6}} = 840 \; \mu\varepsilon. \quad (4)$$

Equation (5) can be used to obtain the tensile elongation in the fiber, where L_0 = 40.0 mm is the initial length of the fiber.

$$\Delta L = L - L_0 = \Delta\varepsilon \; L_0 = 840 \times 10^{-6} \times 40.0 = 0.0336 \text{ mm}. \quad (5)$$

The numerical example shows that corresponding to a water height variation Δh of 12.30 mm, the tensile elongation of the fiber ΔL = 0.0336 mm, which is lower than 0.20 mm (ultimate elongation).

The FBG deformation (tensile elongation) does not represent the settlement of the FBG–DSM sensor. Notably, even if the water flows beneath the bottom surface of the float mass (as depicted in the left sensor in Fig. 4), the fiber does not attain the ultimate tensile strength.

3. Accuracy of measured displacements achieved using the FBG–DSM sensors

A total of 33 three-point bending tests were performed on a compressed steel beam (see Section 3.1) to verify the accuracy of the displacements measured using the FBG–DSM sensors. A comparison of the deflected shape measurements was conducted by positioning a series of dial indicators at the aforementioned cross sections of the FBG–DSM sensors along the beam's length. The tolerance of the dial indicators was identical to that of the FBG–DSM sensors (i.e., 0.01 mm). In the test combinations presented, denoted as Case I, no relaxation occurred in the FBGs inside the sensors because the magnitudes of the prestress forces (in the fiber) were moderate. Corresponding to the maximum obtained displacement of v_3 = 7.07 mm, the tensile elongation of the fiber was approximately 0.0193 mm, which was considerably lower than its ultimate tensile elongation of approximately 0.20 mm. No FBG–DSM sensors were used for temperature compensation because the temperature in the indoor laboratory space was reasonably assumed to be homogenous. The effect of temperature variation on wavelength changes in the FBG–DSM sensors was almost constant. Therefore, wavelength variations among the FBG–

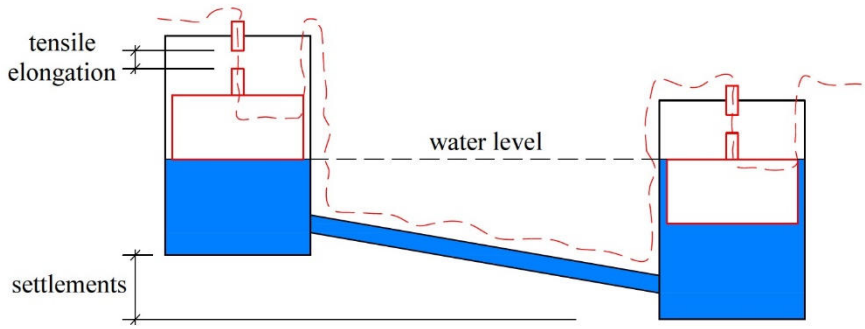

Fig. 4 FBG–DSM sensor system. Water beneath the bottom surface of the float mass (left)

DSM sensors were caused only by vertical deformations (displacements) of the steel beam.

3.1. Static test layout of Case I

A steel beam of 150 mm × 350 mm × 9 mm in a rectangular box cross section was adopted (Fig. 6). The beam was subjected to compressive forces exerted by a strand post-tensioning system. The strand had an eccentricity of 80 mm with respect to the cross section centroid and comprised four tendons with "seven wire strands" of 15.2-mm diameter inserted into four distinct plastic ducts and inside of the box. The plastic ducts were not injected. The ultimate yield strength of the tendons was 1860 MPa. Two supports were placed at the beam ends (Fig. 7(a) and (b)) to create pinned-end restraints, resulting in a clear span L equal to 7.1 m, as shown in Fig. 6. Several steel stiffeners were inserted by welding into the box cross section (Fig. 11(c)) to avoid buckling phenomena in the serviceability state. The cross-sectional second moment of area for the box cross section I_{exact} was 1.334 × 10^8 mm^4 and the slenderness ratio was equal to 57. All geometric dimensions were verified using measuring systems with 0.01-mm tolerance (laser rangefinder and caliper) once the steel beam had been positioned on the supports. Experimental evaluations revealed that the elastic modulus E = 235 GPa, yielding stress f_{yk} = 470 MPa, and ultimate stress f_{uk} = 675 MPa of the C45 steel grade. Based on the tensile tests, the parameters were determined as mean values for three hourglass specimens in accordance with the standards of ASTM International. The employed hydraulic universal machine had a wedge grip, 1000-kN force capacity, and 70-MPa maximum pressure.

The steel beam was inserted into a test frame by using a test rig (Fig. 5(a)). At one beam end, a hydraulic oil jack of 4000-kN force capacity was used to apply a compressive force to pull the strand outward. At the other end, a 1000-kN load cell with 2-mV/V accuracy was positioned to measure the applied compressive force. In total, four compressive loads N_x with values of approximately 299, 370, 448, and 482 kN were assigned. For every assigned compressive force N_x, an additional vertical load F was applied using a hydraulic actuator at the midspan of the beam. The initial value was

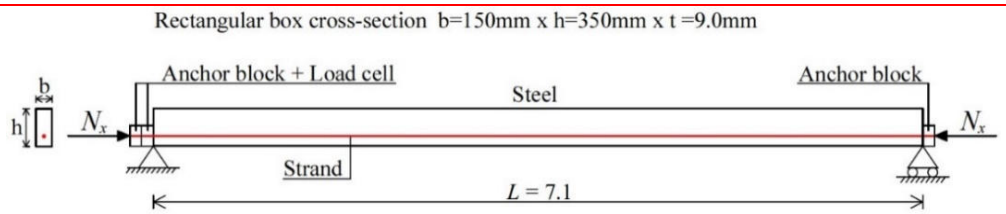

Fig. 6 Scheme of the steel beam specimen. Units in m

(a) Hinge support used for pinned-end constraints

(b) Roller support used for pinned-end constraints

(c) Hydraulic actuator at the midspan

Fig. 7 Steel beam specimen

(a) Test rig of the static tests

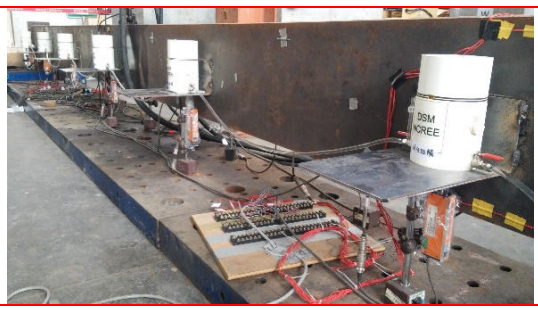

(b) FBG–DSM sensors and dial indicators along the beam's length

Fig. 5. Case I: Steel beam specimen.

approximately 20.0 kN, which gradually increased to approximately 22.5 and 25.0 kN(Fig. 7(c)). The latter test condition was repeated three times, yielding a total of 33 tests.

Seven FBG–DSM sensors and seven dial indicators were positioned along the beam's length corresponding to the cross sections i = 0, ..., 6, based on the test layout depicted in Figs. 5(a) and 8. Steel plates were used to locate each sensor corresponding to the beam axis (Fig. 5(b)). The dial indicators were connected to a data logger located on a desk close to the test rig. The FBG–DSM sensors were connected by optical wires along the beam span and linked by a connecting pipe. Two additional reference FBG–DSM sensors, labeled "R.F." in Fig. 8, were placed on two distinct tables on the gr ound (Fig. 5(a)). A static full spectrum optical interrogator positioned on the ground was used as the data logger to acquire the FBG–DSM signals. Similarly, the ground floor was used as the reference for dial indicator measurements.

All test measurements were recorded every second for nearly 200 seconds by a data acquisition unit. The average measurements of the compressive forces N_x and loads F for each test combination are listed in Table 2.

3.2. Comparison of measured displacements

Using the FBG–DSM sensors and dial indicators, the short-term displacements v_i for i = 0, ..., 6 were measured at the seven cross sections (Fig. 8) every second for nearly 200 seconds by a data acquisition unit. Table 2 shows the displacement measurements obtained from one test

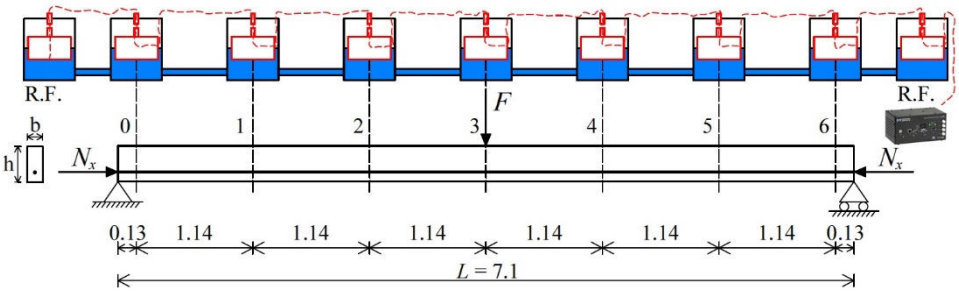

Fig. 8 Case I: Test layout with locations of the instrumented sections of the FBG–DSM sensing system. Units in mm

Table 2 Case I: Comparison of measured displacements corresponding to the test layout depicted in Fig. 8

	N_x (kN)	F (kN)	v_0 (mm)	v_1 (mm)	v_2 (mm)	v_3 (mm)	v_4 (mm)	v_5 (mm)	v_6 (mm)
Dial indicator	300	19.9	0.63	3.47	4.79	5.48	4.70	2.82	0.37
FBG–DSM			0.69	2.98	4.78	5.43	4.72	2.86	0.47
Dial indicator	300	22.3	0.72	3.85	5.38	6.17	5.30	3.17	0.41
FBG–DSM			0.76	3.33	5.37	6.10	5.31	3.20	0.51
Dial indicator	371	19.8	0.59	3.42	4.81	5.50	4.75	2.81	0.35
FBG–DSM			0.67	3.00	4.81	5.48	4.76	2.89	0.42
Dial indicator	371	22.3	0.67	3.81	5.39	6.16	5.32	3.15	0.38
FBG–DSM			0.75	3.35	5.39	6.14	5.33	3.23	0.46
Dial indicator	371	24.8	0.63	4.15	5.97	6.86	5.92	3.51	0.44
FBG–DSM			0.77	3.68	6.15	6.86	5.90	3.58	0.51
Dial indicator	447	19.8	0.73	3.50	4.89	5.59	4.84	2.90	0.41
FBG–DSM			0.72	3.05	4.86	5.55	4.83	2.96	0.47
Dial indicator	447	22.3	0.90	3.95	5.56	6.35	5.50	3.31	0.50
FBG–DSM			0.84	3.47	5.53	6.29	5.49	3.38	0.57
Dial indicator	448	24.8	1.02	4.48	6.26	7.21	6.22	3.79	0.60
FBG–DSM			0.87	3.84	6.19	7.07	6.16	3.83	0.72
Dial indicator	482	19.8	0.61	3.46	4.74	5.43	4.67	2.78	0.32
FBG–DSM			0.71	3.05	4.81	5.47	4.79	2.92	0.44
Dial indicator	482	22.3	0.61	3.46	4.74	5.43	4.67	2.78	0.32
FBG–DSM			0.78	3.41	5.40	6.14	5.39	3.27	0.49
Dial indicator	482	24.7	0.74	4.22	5.92	6.79	5.84	3.48	0.41
FBG–DSM			0.84	3.75	5.98	6.80	5.98	3.62	0.53
Mean error (mm)			**0.05**	**-0.44**	**0.07**	**0.03**	**0.08**	**0.11**	**0.10**
Mean relative error (%)			**0.09**	**-0.12**	**0.02**	**0.01**	**0.02**	**0.04**	**0.25**

combination. The repetition of each test combination provided favorable repeatability, yielding a relative error of less than 0.5% between all (repeated) measures. In particular, the displacements v_i were recorded after applying the vertical load F and considering the assigned compressive force N_x as the initial displacement reference condition. The test combination with N_x = 299 kN and F = 25.0 kN was neglected for a temporary lack of accuracy in the load F measurement. Notably, every single combination of compressive force N_x and load F preserved the steel beam in the elastic range.

The absolute mean error between the measured displacements v_2, v_3, and v_4, excluding the test combination with N_x = 482 kN and F = 22.3 kN, was equal to 0.04 mm corresponding to a relative error of 0.8%. The measured displacements v_1 exhibited a systematic error equal to a mean value of –0.44 mm due to a dial indicator malfunction. The symmetric displacement v_5 was characterized by a mean error of 0.11 mm and corresponded to a relative error of 3.8%. The measured displacements v_0 and v_6 close to the end constraints and characterized by few tenths of a millimeter yielded an absolute mean error of 0.09 mm. Nonetheless, excluding the measured displacement v_1, the absolute mean error of all measures was lower than 0.08 mm, irrespective of the rotation to which the bases of the FBG–DSM sensors were subjected. The mean errors of each v_i for i = 0, ..., 6 in Case I are summarized at the bottom of Table 2.

4. Static NDT method for compressive force detection

The formulation of the new static NDT method is illustrated in Fig. 9, and considers a simply supported compressed beam of length L. The prismatic member is subjected to an eccentrically compressive force N (with eccentricity e) with respect to the cross section centroid (Fig. 9(a)) and a vertical load F located at the midspan (Fig. 9(b)). The compressive force N is assumed to be externally applied. The elastic modulus E of steel and cross-sectional second moment of area I are assumed to be known constants.

The initial deflection curve $v^{(0)}$ (Fig. 9(a)) after the eccentrically compressive load N has been applied is expressed as follows (Timoshenko and Gere 1961, Bazant and Cedolin 1991):

$$v^{(0)}(x) = e\left[1-\cos\sqrt{n}\left(\frac{1}{2}-\frac{x}{L}\right)\Big/\cos(\sqrt{n}/2)\right], \tag{6}$$

where $n = NL^2 / EI$ is the nondimensional axial force. Subsequently, a point load F is applied to the initial deflection curve $v^{(0)}$; the corresponding bending moments in the left and right portions of the beam in Fig. 9(b) are respectively expressed as follows:

$$M = F\,x/2 + N\,(v^{(1)} - e) \;\text{ for }\; 0 \le x \le L/2, \tag{7a}$$

$$M = F\,(L-x)/2 + N\,(v^{(1)} - e) \;\text{ for }\; L/2 \le x \le L. \tag{5b}$$

Substituting Eq. 7(a) and (b) in the expression for the curvature of the beam axis $M = -EI\ \mathrm{d}^2v^{(1)} / \mathrm{d}x^2$ yields the solution $v^{(1)} = v^{(0)} + v_{\mathrm{tot}}^{(a)}$, where $v_{\mathrm{tot}}^{(a)}$ is the deflection curve of the beam under the concentric axial load N and vertical load F (Fig. 9(c); Timoshenko and Gere 1961, Bazant and Cedolin 1991, Tullini 2013), expressed as follows:

$$v_{\mathrm{tot}}^{(a)}(x) = \frac{\psi}{2\sqrt{n^3}}\left[\frac{1}{\cos\sqrt{n}/2}\sin\left(\sqrt{n}\,\frac{x}{L}\right)-\sqrt{n}\,\frac{x}{L}\right] \;\text{ for } 0 \le x \le L/2, \tag{8a}$$

$$v_{\mathrm{tot}}^{(a)}(x) = \frac{\psi}{2\sqrt{n^3}}\left\{\frac{1}{\cos\sqrt{n}/2}\sin\left[\sqrt{n}\left(1-\frac{x}{L}\right)\right]-\sqrt{n}\left(1-\frac{x}{L}\right)\right\} \;\text{ for } L/2 \le x \le L, \tag{8b}$$

$\psi = FL^3 / EI$ is the load parameter with a length dimension.

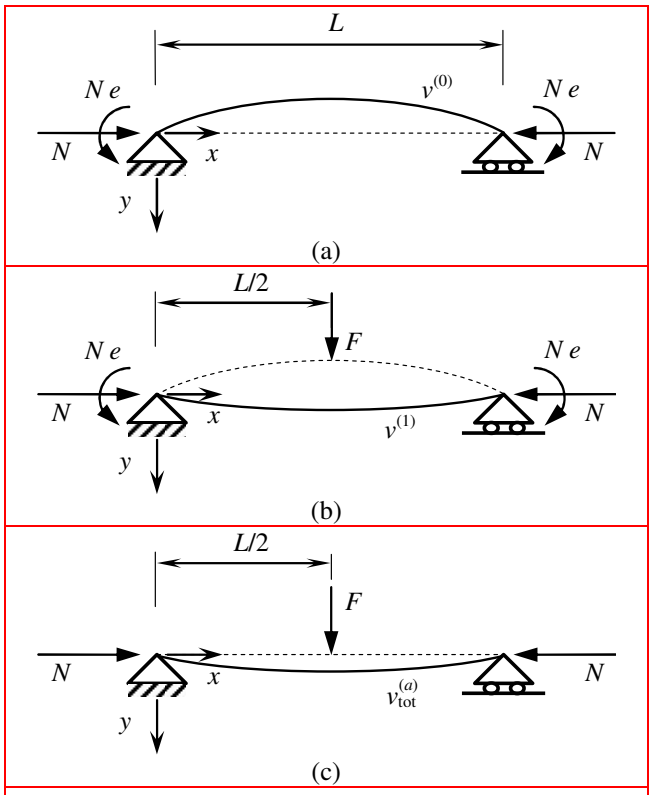

Fig. 9 Reference model of the compressed steel beam. Deflection curve $v^{(0)}$ after eccentric compressive load N has been applied (a), deflection curve $v^{(1)}$ after load F has been applied to deflection curve $v^{(0)}$ (b), and deflection curve $v_{\mathrm{tot}}^{(a)}$ after load F (c) has been applied. The dashed lines correspond to the initial deflection curves

The measured deflections in the experiments conducted in this study were compared with the analytical solution $v_{\mathrm{tot}}^{(a)} = v^{(1)} - v^{(0)}$ generated by Eq. 8(a) and (b). As n approaches zero, the limit of Eq. (8) yields the first-order displacement $v_{\mathrm{I}}^{(a)}$

(neglecting the effect of the external compressive load), expressed as follows:

$$v_{\mathrm{I}}^{(a)}(x)=\frac{\psi}{12}\frac{x}{L}\left[\frac{3}{4}-\left(\frac{x}{L}\right)^2\right] \quad \text{for } 0\le x\le L/2, \tag{9a}$$

$$v_{\mathrm{I}}^{(a)}(x)=\frac{\psi}{12}\left(1-\frac{x}{L}\right)\left[\frac{2x}{L}-\left(\frac{x}{L}\right)^2-\frac{1}{4}\right] \quad \text{for } L/2 \le x\le L. \tag{9b}$$

The total vertical displacement in Eq. (8) is well approximated by the first-order deflection reported in Eq. (9) multiplied by the magnification factor of the second-order effects $1/(1-N/N_{\mathrm{crE}})$ (Timoshenko and Gere 1961, Bazant and Cedolin 1991), expressed as follows:

$$v_{\mathrm{tot}}^{(x)}(x)=\frac{v_{\mathrm{I}}^{(a)}(x)}{1-N/N_{\mathrm{crE}}}, \tag{10}$$

where $N_{\mathrm{crE}} = \pi^2 EI / L^2$ is the first Euler buckling load for a simply supported beam. Thus, the magnification factor of the second-order effects coincides with the ratio $v_{\mathrm{I}}^{(a)}(x)/v_{\mathrm{tot}}^{(x)}(x)$. During the execution of preliminary design computations, a n approximation of Eq. (10) can be performed to determine the displacements in the compressed steel beams.

A three-point bending test with assigned compressive force N can be conducted to measure the vertical displacement $v_{\mathrm{tot}}^{(x)}(x)$. Consequently, the ratio $v_{\mathrm{I}}^{(a)}(x)/v_{\mathrm{tot}}^{(x)}(x)$ and definition of the magnification factor can be used to identify the compressive load N_a in steel beam columns with the following relation (Bonopera *et al.* 2018):

$$N_a = N_{\mathrm{crE}}\left(1-\frac{v_{\mathrm{I}}^{(a)}(x)}{v_{\mathrm{tot}}^{(x)}(x)}\right). \tag{11}$$

By substituting the nondimensional axial force $n_a = N_a L^2/EI$, Eq. (11) can be reduced to

$$n_a = \pi^2\left(1-\frac{v_{\mathrm{I}}^{(a)}(x)}{v_{\mathrm{tot}}^{(x)}(x)}\right). \tag{12}$$

When the point load F is applied at the midspan, Eq. 9(a) yields the first-order displacement at a quarter of the span, $v_{\mathrm{I}}^{(a)}(L/4) = 11\psi/768$, as well as the first-order midspan deflection by using the expression, $v_{\mathrm{I}}^{(a)}(L/2) = \psi/48$. In this cases, Eq. (12) can be reduced to

$$n_a=\pi^2\left(1-\frac{11\psi}{768\, v_{\mathrm{tot}}^{(x)}(L/4)}\right) \quad \text{or}$$

$$n_a=\pi^2\left(1-\frac{\psi}{48\, v_{\mathrm{tot}}^{(x)}(L/2)}\right). \tag{13a, b}$$

In summary, load identification must conform to the following steps:

(1) Measure the displacement at the quarter cross section $v_{\mathrm{tot}}^{(x)}(L/4)$ along the beam's length following the application of load F, or alternatively, measure the corresponding displacement at the midspan $v_{\mathrm{tot}}^{(x)}(L/2)$.

(2) Solve Eq. 13(a) or (b) for the unknown constant n_a by using the displacement $v_{\mathrm{tot}}^{(x)}(L/4)$ or $v_{\mathrm{tot}}^{(x)}(L/2)$, as well as the expression for ψ.

(3) Determine the analytical value $N_a = n_a\, EI / L^2$ of the compressive force.

Notably, the additional load F can be located at various cross sections, thereby underlining that the first-order displacement $v_{\mathrm{I}}^{(a)}(x_i)$ and experimental displacement $v_{\mathrm{tot}}^{(x)}(x_i)$ must be in reference to the same cross section. Various boundary conditions can be considered by assuming the appropriate Euler buckling load N_{crE} in Eq. (10). The end constraints of a steel beam are often known, and the end stiffness of these elements can be measured experimentally *in situ* or obtained from the construction project drawings. With respect to space roof trusses where the internal joint stiffness is extremely difficult to identify, investigations on unloaded space structures will be conducted in subsequent studies.

4.1. Static test layout of Case II

The steel beam described in Section 3.1 was adopted (Fig. 6) with consideration of the test layout depicted in Figs. 10 (Case II) and 11(a). In this case, two additional reference FBG–DSM sensors labeled "R.F." in Fig. 10 were positioned at the beam ends (Fig. 11(b)) to form a reference line for the displacement measurement system between the pinned-end constraints. Steel plates were utilized to locate each FBG–DSM sensor corresponding to the beam length (Fig. 11(b)). Similar to Case I, none of the FBG–DSM sensors were used for temperature compensation.

A preliminary three-point bending test was conducted to measure the first-order midspan displacement v_3. The load F at the midspan was equal to 2.5 kN, whereas a compressive force N_x of approximately 21 kN was applied to preserve the steel beam without second-order effects. Using the expression $v_3 = \psi / 48$, the same elastic modulus E of the tensile tests was gained. Cases I and II were concurrently performed. Notably, all test measurements were recorded every second for nearly 200 seconds by a data acquisition unit. The average measurements of the corresponding compressive forces N_x, loads F, and displacements v_i for each test combination are shown in Table 3. Corresponding to the maximum measured displacement v_3 = 6.39 mm, the tensile elongation of the fiber was approximately 0.0175 mm. In addition, favorable repeatability of the measurements was obtained for each test combination of Case II, yielding a relative error of less than 0.5% between all measures (repeated three times). The repetitions resulted in a total of 24 tests. The experiments with N_x = 482 kN were neglected because of contact between the tendons and steel stiffeners, which modified the original horizontal action line of the compressive load N_x. The steel beam was preserved in the elastic range throughout the aforementioned experiments.

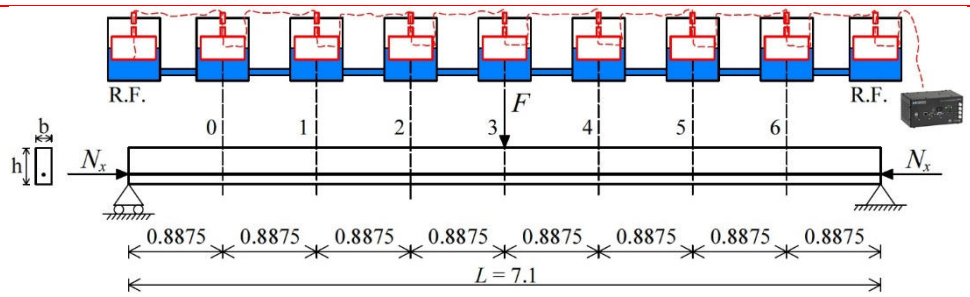

Fig. 10 Case II: Test layout with locations of the instrumented sections based on the FBG–DSM sensing system. Units in m

(a) Layout of FBG–DSM sensors

(b) Reference FBG–DSM sensor at one beam end

(c) PVC ducts of tendons crossing one steel stiffener

Fig. 11 Case II: Steel beam specimen

The Euler buckling load of the beam $N_{\mathrm{crE}} = \pi^2 E\, I_{exact} / L^2$ = 6138 kN. Thus, the maximum compressive force of N_x = 448 kN, assigned in Case II, was only 7.3% of N_{crE}. Consequently, first-order displacements were magnified by a factor lower than 1 / (1 – 0.073) = 1.08. This small magnification factor requires highly accurate displacement measurements because second-order effects are usually neglected when the magnification factor is lower than 1.10.

Table 3 compares the average displacement measurements v_i of the instrumented sections with the corresponding numerical values $v_{\mathrm{tot}}^{(a)}(x)$ from Eq. (8) and the elastic modulus of E = 235 GPa. Moreover, Table 3 lists the average measurements of the applied compressive forces N_x and loads F. The absolute mean error between the analytical and measured displacements v_2, v_3, and v_4 was 0.03 mm, corresponding to a relative error of 0.5%. The measured displacements v_5 exhibited a mean difference of –0.10 mm, whereas the symmetric displacement v_1 was characterized by a mean error of –0.05 mm, corresponding to a relative error of –1.2%. The measured displacement v_6 close to the end support exhibited a mean difference of –0.20 mm, whereas the mean error of the symmetric displacement v_0 was equal to –0.03 mm, corresponding to a relative error of –1.6%. Excluding the measured displacement v_6, the absolute mean error of all measures was lower than 0.04 mm. The mean errors of each v_i for i = 0, ..., 6 in Case II are summarized at the bottom of Table 3.

The FBG–DSM sensor system was effective in the present study. Figure 12 shows the factor $1 - v_{\mathrm{tot}}^{(a)} / v_i$ for i = 1, 2, and 3. A maximum error of –4.1% was recorded for the nine tests with N_x = 371 kN. The values $v_{\mathrm{tot}}^{(a)}(x)$ were similarly obtained from Eq. (8). The errors decreased considerably in the larger compressive loads N_x and displacements v_2 and v_3 close to and at the midspan, respectively.

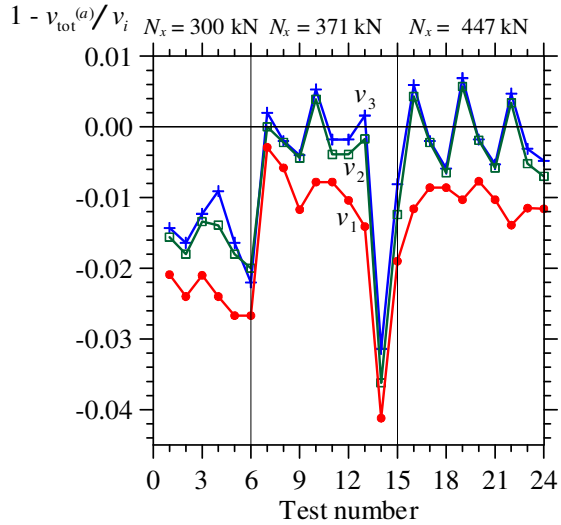

Fig. 12 Error $1 - v_{\mathrm{tot}}^{(a)} / v_i$ versus test number for all test combinations and displacements v_1, v_2, and v_3 depicted in Fig. 10

4.2. Compressive force detections

Evaluations of the compressive nondimensional forces n_a are presented in Table 4. In particular, the detections were obtained by using the experimental values of $\psi = FL^3 / EI_{exact}$

Table 3 Case II: Comparison between the analytical and measured displacements corresponding to the test layout depicted in Fig. 10

	N_x (kN)	F (kN)	v_0 (mm)	v_1 (mm)	v_2 (mm)	v_3 (mm)	v_4 (mm)	v_5 (mm)	v_6 (mm)
Analytical	300	19.9	1.83	3.42	4.55	4.97	4.55	3.42	1.83
FBG–DSM			1.77	3.35	4.48	4.90	4.47	3.27	1.60
Analytical	300	22.3	2.05	3.84	5.10	5.57	5.10	3.84	2.05
FBG–DSM			1.98	3.75	5.03	5.52	5.03	3.69	1.81
Analytical	371	19.8	1.84	3.45	4.58	5.01	4.58	3.45	1.84
FBG–DSM			1.83	3.44	4.58	5.02	4.58	3.38	1.67
Analytical	371	22.3	2.08	3.88	5.16	5.64	5.16	3.88	2.08
FBG–DSM			2.05	3.85	5.14	5.63	5.15	3.79	1.87
Analytical	371	24.8	2.31	4.32	5.74	6.27	5.74	4.32	2.31
FBG–DSM			2.25	4.26	5.73	6.28	5.74	4.22	2.09
Analytical	447	19.8	1.87	3.50	4.64	5.07	4.64	3.50	1.87
FBG–DSM			1.86	3.47	4.63	5.06	4.63	3.42	1.70
Analytical	447	22.3	2.10	3.94	5.23	5.72	5.23	3.94	2.10
FBG–DSM			2.10	3.91	5.22	5.71	5.21	3.85	1.91
Analytical	448	24.8	2.34	4.38	5.81	6.36	5.81	4.38	2.34
FBG–DSM			2.32	4.32	5.83	6.39	5.84	4.34	2.20
Mean error (mm)			**-0.03**	**-0.05**	**-0.02**	**-0.01**	**-0.02**	**-0.10**	**-0.20**
Mean relative error (%)			**-0.02**	**-0.01**	**0.00**	**0.00**	**0.00**	**-0.03**	**-0.10**

and v_1 in Eq. 13(a) or the same parameter ψ and v_3 in Eq. 13(b) for each test combination. Table 4 shows the experimental and estimated parameters of the load identification procedure by the quarter displacement v_1 and midspan displacement v_3. The elastic modulus of E = 235 GPa was utilized as a parameter in the procedure. The percentage errors $\Delta = (N_a - N_x) / N_x$ are also illustrated. The tests exhibited excellent compressive load N_a detections when N_x > 371 kN, particularly when the beam was subjected to compressive forces N_x, yielding second-order effects greater than 6% of the total displacements. When the quarter displacements v_1 were used, the estimates N_a deteriorated for all experiments.

Sensitivity analyses were performed to verify the test results. The values v_1 and v_3 obtained by Eq. (8) and parameter ψ were modified to reproduce possible experimental errors. In particular, the values v_1, v_3, and ψ were alternatively multiplied by 0.99 and 1.01, resulting in s even combinations of simulated values for seven distinct assumed compressive loads N_x. The maximum load of F = 25.0 kN in the experiments was assumed in the process because the load estimations calculated using Eq. 13(a) and (b) did not depend on the vertical load magnitude. Fig. 13(a) and (b) exhibited the comparison between the worst estimated N_a and assumed N_x values by using displacements v_1 and v_3; both cases yielded a constant error of approximately ±60 kN. The comparison between the measured N_x and estimated N_a values generated in the experiments (Table 4) is detailed in Fig. 13(a) and (b). Favorable correspondence between the analytical and experimental identifications was gained when the midspan

Table 4 Case II: Compressive force detections. The superscript * and subscript a refer to the measured and estimated parameters using displacements v_1 and v_3, respectively

		Displacements v_1				Displacements v_3			
N_x^* (kN)	F^* (kN)	ψ/v_1^*	n_a	N_a (kN)	Δ_a (%)	ψ/v_3^*	n_a	N_a (kN)	Δ_a (%)
300	19.9	67.8	0.28	176	-41.5	46.4	0.34	209	-30.4
300	22.3	67.9	0.27	169	-43.6	46.1	0.39	240	-20.0
371	19.8	65.7	0.58	361	-2.8	45.0	0.61	380	2.3
371	22.3	66.1	0.52	324	-12.6	45.2	0.57	355	-4.3
371	24.8	66.5	0.47	295	-20.6	45.1	0.60	373	0.4
447	19.8	65.1	0.66	411	-8.1	44.7	0.68	425	-4.9
447	22.3	65.1	0.66	413	-7.5	44.6	0.70	436	-2.4
448	24.8	65.5	0.60	376	-16.1	44.3	0.76	472	5.3

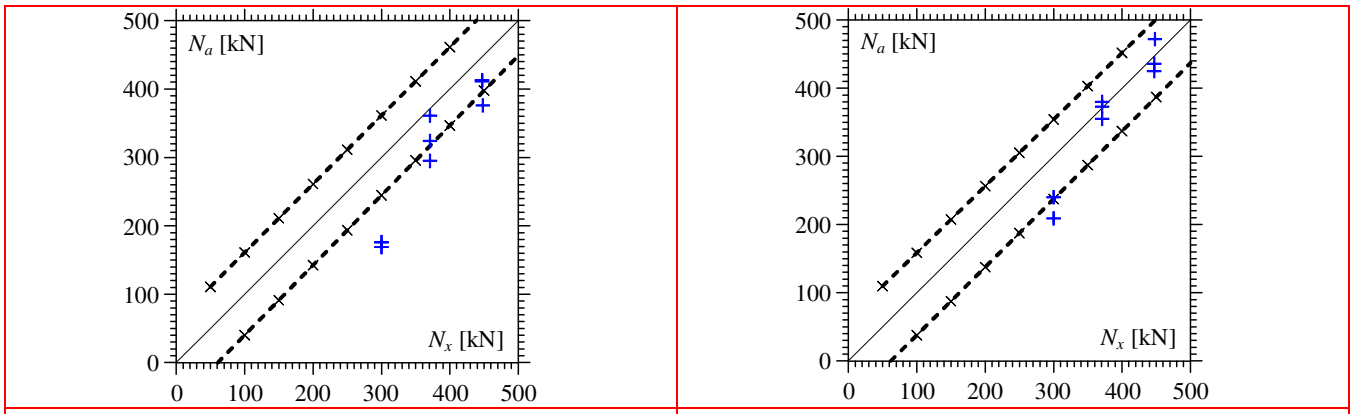

(a) Force detections based on Eq. (13a). (b) Force detections based on Eq. (13b).

Fig. 13 Case II: Comparison between estimated N_a and measured N_x values using displacements v_1 (a) and v_3 (b). The dashed lines with × refer to the sensitivity analyses; + refers to the experimental data

displacement v_3 was considered because of its greater second-order effects.

The method proposed by Tullini *et al.* (2012) was adopted to identify the prestress forces N_a by using the measured displacements in Case II (Fig. 10). This method is able to detect the axial force in externally loaded elements with known geometric and elastic properties, idealized as simply supported Euler–Bernoulli beams. The application of an additional load F at the midspan of the element is necessary for measuring the displacements at three given cross sections along the beam axis. Two test configurations were considered, both of which had a substructure length of L = 7.1 m (Fig. 10). One test employed the three sensors located at cross sections i = 1, 3, and 5. By contrast, the other test considere d the short-term displacements v_2, v_3, and v_4 (Table 3). The estimation errors $\Delta = (N_a - N_x) / N_x$ were unsatisfactory for both configurations.

5. Conclusions

This paper presents the performance of a novel static NDT method that can detect the compressive load in steel members. If the beam's flexural rigidity is identified, the compressive force can be deduced using the midspan displacement recorded accurately in a three-point bending test. Therefore, the deflected shape of a compressed steel beam was short-term measured using a series of FBG–DSM sensors in several laboratory tests. The high accuracy of the midspan deflections using the FBG–DSM sensor measuring system yielded excellent load detection. Compressive forces that induce a magnification factor greater than 1.06 are required to obtain identification errors lower than 10%. The method proposed by Tullini *et al.* (2012) yielded unsatisfactory approximations of the compressive forces, even when accurate measurements from the FBG–DSM sensors were used. These results confirm the applicability of the method proposed by Tullini *et al.* (2012) for members with high slenderness only. The new static method enables reliable load identification in steel beams with low slenderness. Moreover, in contrast to Bonopera *et al.* (2018), evaluation of the first-order displacement through use of the magnification factor formula (Eq. (11)) is not required. Finally, the new method can be applied *in situ* to generically compressed steel beams after the stiffness of the corresponding boundary conditions had been investigated. Thus, the FBG–DSM sensors (Lee 2014, 2015) have the pot ential for easy measurement system installation along the top chords of space trusses.

Acknowledgments

M.B. acknowledges the financial support of the "Tender for Young Researchers Abroad Grant" in 2014, provided by the University of Ferrara, Italy, and the "Summer Program in Taiwan Grant" in 2014 and 2015, provided by the Ministry of Science and Technology of Taiwan for European Ph.D. candidates. N.T. acknowledges the financial support of the "Research Program FAR 2017" provided by the University of Ferrara. The experiments were supported by funding from the National Applied Research Laboratories Project of Taiwan (NCREE-06104A1700). Finally, special gratitude is extended to the technicians of National Center for Research on Earthquake Engineering and students of National Taiwan University, who provided considerable assistance to the authors.

References

Aldar, A. (Ed.) (2013), *Health assessment of engineered structures: bridges, buildings, and other infrastructures*, World Scientific Publishing.

Bahra, A.S. and Greening, P.D. (2011), "Identifying multiple axial load patterns using measured vibration data", *J. Sound Vib.*, **330**(15), 3591–3605.

Bazant, Z.P. and Cedolin, L. (1991), *Stability of Structures*, Oxford University Press, New York.

Bonopera, M., Chang, K.C., Chen, C.C., Lin, T.K. and Tullini, N. (2018), "Compressive column load identification in steel space

frames using second-order deflection-based methods", *Int. J. Struct. Stab. Dy.*, **18**(8) 1850092. DOI: 10.1142/S021945541850092X

Chang, K.C., Lee, Z.K. and Chen, C.C. (2012), "Structural assessment of a repaired cable bridge damaged in 1999 Chi-Chi earthquake", *Proceedings of the International Symposium on Engineering Lessons Learned from the 2011 Great East Japan Earthquake*, March 1–4, Tokyo, Japan.

International Federation for Structural Concrete (2003), Monitoring and safety evaluation of existing concrete structures, FIB Bulletin No. 22, Lausanne, Switzerland.

Kim, Y.S., Sung, H.J., Kim, H.W. and Kim, J.M. (2011), "Monitoring of tension force and load transfer of ground anchor by using optical FBG sensors embedded tendon", *Smart Struct. Syst.*, **7**(4), 303–317.

Lai, C.C., Au, H.Y., Liu, M.S.Y., Ho, S.L. and Tam, H.Y. (2016), "Development of level sensors based on fiber Bragg grating for railway track differential settlement measurement", *IEEE Sens. J.*, **16**(16), 6346–6350.

Lee, Z.K. (2013), "Dazhi bridge safety monitoring demonstration project", *Proceedings of the 5th International Conference on Advances in Experimental Structural Engineering*, November 8–9, Taipei, Taiwan.

Lee, Z.K, Chen, C.C., Hung, H.H., Sung, Y.C., Lee, L.S. (2014), "Loading tests and long-term monitoring on Wugu-Yangmei viaduct of Taiwan National Highway", *Proceedings of the 5th Asia Conference on Earthquake Engineering*, October 16–18, Taipei, Taiwan.

Lee, Z.K. (2014), Bridge safety monitoring integrated system with full optical fiber and the method for sensing thereof, *J.P. Patent No. 5542980*.

Lee, Z.K. (2015), Bridge safety monitoring integrated system with full optical fiber and the method for sensing thereof, *U.S. Patent No. 9183739*.

Lim, Y.Y. and Soh, C.K. (2013), "Damage detection and characterization using EMI technique under varying axial load", *Smart Struct. Syst.*, **11**(4), 349–364.

Maes, K., Peeters, J., Reynders, E., Lombaert, G. and De Roeck, G. (2013), "Identification of axial forces in beam members by local vibration measurements", *J. Sound Vib.*, **332**(21), 5417–5432.

Marecos, J. (1978), "The measurement of vertical displacements through water levelling method", *Mater. Struct.*, **11**(5), 361–370.

Naseralavi, S.S., Shojaee, S. and Ahmadi, M. (2016), "Modified gradient methods hybridized with Tikhonov regularization for damage identification of spatial structure", *Smart Struct. Syst.*, **18**(5), 839–864.

Rebecchi, G., Tullini, N. and Laudiero, F. (2013), "Estimate of the axial force in slender beams with unknown boundary conditions using one flexural mode shape", *J. Sound Vib.*, **332**(18), 4122–4135.

Rodrigues, C., Felix, C., Lage, A. and Figueiras, J. (2010), "Development of a long-term monitoring system based on FBG sensors applied to concrete bridges", *Eng. Struct.*, **32**(8), 1993–2002.

Rodrigues, C., Felix, C. and Figueiras, J. (2011), "Fiber-optic-based displacement transducer to measure bridge deflections", *Struct. Health Monit.*, **10**(2), 147–156.

Sung, H.J., Do, T.M., Kim, J.M. and Kim, Y.S. (2017), "Long-term monitoring of ground anchor tensile forces by FBG sensors embedded tendon", *Smart Struct. Syst.*, **19**(3), 269–277.

Timoshenko, S.P. and Gere, J.M. (1961), *Theory of Elastic Stability*, McGraw–Hill, New York.

Tullini, N. and Laudiero, F. (2008), "Dynamic identification of beam axial loads using one flexural mode shape", *J. Sound Vib.*, **318**(1–2), 131–147.

Tullini, N., Rebecchi, G. and Laudiero, F. (2012), "Bending tests to estimate the axial force in tie-rods", *Mech. Res. Commun.*, **44**, 57–64.

Tullini, N. (2013), "Bending tests to estimate the axial force in slender beams with unknown boundary conditions", *Mech. Res. Commun.*, **53**, 15–23.

Vurpillot, S., Krueger, G., Benouaich, D., Clément, D. and Inaudi, D. (1998), "Vertical deflection of a pre-stressed concrete bridge obtained using deformation sensors and inclinometer measurements", *ACI Struct. J.*, **95**(5), 518–526.